Journal of the American College of Cardiology
© 2005 by the American College of Cardiology Foundation
Published by Elsevier Inc.

Vol. 45, No. 12, 2005
ISSN 0735-1097/05/$30.00
doi:10.1016/j.jacc.2005.03.029

**PRECLINICAL RESEARCH**

# Real-Time Magnetic Resonance-Guided Endovascular Repair of Experimental Abdominal Aortic Aneurysm in Swine

Venkatesh K. Raman, MD,* Parag V. Karmarkar, MSc,*‡ Michael A. Guttman, MSc,† Alexander J. Dick, MD,* Dana C. Peters, PhD,† Cengizhan Ozturk, MD, PhD,* Breno S. S. Pessanha, MD,* Richard B. Thompson, PhD,† Amish N. Raval, MD,* Ranil DeSilva, MBBS, PhD,* Ronnier J. Aviles, MD,* Ergin Atalar, PhD,‡ Elliot R. McVeigh, PhD,† Robert J. Lederman, MD*

*Bethesda and Baltimore, Maryland*

**OBJECTIVES** This study tested the hypotheses that endografts can be visualized and navigated in vivo solely under real-time magnetic resonance imaging (rtMRI) guidance to repair experimental abdominal aortic aneurysms (AAA) in swine, and that MRI can provide immediate assessment of endograft apposition and aneurysm exclusion.

**BACKGROUND** Endovascular repair for AAA is limited by endoleak caused by inflow or outflow malapposition. The ability of rtMRI to image soft tissue and flow may improve on X-ray guidance of this procedure.

**METHODS** Infrarenal AAA was created in swine by balloon overstretch. We used one passive commercial endograft, imaged based on metal-induced MRI artifacts, and several types of homemade active endografts, incorporating MRI receiver coils (antennae). Custom interactive rtMRI features included color coding the catheter-antenna signals individually, simultaneous multislice imaging, and real-time three-dimensional rendering.

**RESULTS** Eleven repairs were performed solely using rtMRI, simultaneously depicting the device and soft-tissue pathology during endograft deployment. Active devices proved most useful. Intraprocedural MRI provided anatomic confirmation of stent strut apposition and functional corroboration of aneurysm exclusion and restoration of laminar flow in successful cases. In two cases, there was clear evidence of contrast accumulation in the aneurysm sac, denoting endoleak.

**CONCLUSIONS** Endovascular AAA repair is feasible under rtMRI guidance. Active endografts facilitate device visualization and complement the soft tissue contrast afforded by MRI for precise positioning and deployment. Magnetic resonance imaging also permits immediate postprocedural anatomic and functional evaluation of successful aneurysm exclusion. (J Am Coll Cardiol 2005;45:2069–77) © 2005 by the American College of Cardiology Foundation

Endovascular repair is an alternative to open surgery that is emerging as an elective treatment for abdominal aortic aneurysm (AAA) (1–3). An important complication of endovascular AAA repair is endoleak, a persistent systemic communication with the aneurysm sac that risks continued expansion and rupture. Of the types described by White et al. (4), type I endoleak results from an incomplete seal at the proximal or distal attachment site of the endograft. This has been reported in up to 25% of cases (5–8) in older series, and may be caused by device misposition, stent malapposition, and device undersizing (9) or oversizing (10). Better soft tissue visualization and depiction of complex three-dimensional (3D) anatomy by interactive magnetic resonance imaging (MRI) may limit this complication.

Magnetic resonance imaging may be equivalent or superior to X-ray computed tomography for procedure planning and surveillance after endograft placement (11–13). Real-time MRI (rtMRI) can guide clinical invasive procedures (14) and pre-clinical interventions, such as transcatheter repair of intracardiac shunt (15,16) and endomyocardial injection of therapeutic agents (17). An MRI permits 3D tissue and hemodynamic characterization, creating opportunities to improve endovascular aneurysm treatment and to limit procedural failure from type I endoleak. We hypothesize that: 1) endografts can be visualized and navigated in vivo solely under rtMRI to repair experimental AAA in swine; 2) MRI can provide useful intraprocedural information about anatomy and guide device placement; and 3) MRI can provide immediate confirmation of successful endograft apposition and aneurysm exclusion.

## METHODS

**Animal preparation and aneurysm model.** Animal protocols were approved by the National Heart, Lung, and Blood

From the *Cardiovascular Branch and the †Laboratory of Cardiac Energetics, Division of Intramural Research, National Heart, Lung, and Blood Institute, Bethesda, Maryland; and the ‡Department of Radiology, Johns Hopkins University School of Medicine, Baltimore, Maryland. Supported by NIH Z01-HL005062-01CVB (to Dr. Lederman). Drs. Raman and Karmarkar contributed equally to this work.

Manuscript received May 24, 2004; revised manuscript received February 20, 2005, accepted March 1, 2005.

JACC Vol. 45, No. 12, 2005
June 21, 2005:2069–77

**Abbreviations and Acronyms**

3D = three dimensional
AAA = abdominal aortic aneurysm
MRA = magnetic resonance angiography
MRI = magnetic resonance imaging
rFOV = reduced field of view
SSFP = steady state free precession MRI
TE = echo time
TR = repetition time

Institute Animal Care and Use Committee. Eleven Yorkshire swine (Animal Biotech Industries, Danboro, Pennsylvania) or National Institutes of Health mini-swine (National Institutes of Health Veterinary Resource Program, Poolesville, Maryland) weighing 60 to 85 kg were studied. Anesthesia was induced with ketamine/xylazine and maintained with inhaled isoflurane. Nonferrous 12-F sheaths (Check Flo II, Cook, Bloomington, Indiana) were placed percutaneously in the femoral artery. Animals underwent anticoagulation with a heparin 100-IU/kg bolus dose and a 40- to 60-IU/kg/h infusion.

We modified an acute nonsurgical model of AAA (18). Vessels were sized by X-ray digital subtraction aortography using a marker pigtail catheter. Single, double, or triple overlapping balloons (XXL, 14- to 18-mm diameter × 20-mm length, Boston Scientific/Medi-Tech, Natick, Massachusetts; and AgilTrac, 10- to 14-mm diameter × 20-mm length, Guidant, Menlo Park, California) were inflated for up to 10 min within the infrarenal aorta to achieve an overstretch ratio of at a least 2:1. This was repeated until the dilated segment was at least 1.5 times the reference diameter or until dissection or rupture.

**Construction of endograft devices.** Different self-expanding endograft designs were tested, including one passive device and three different active designs. *Passive* refers to device visibility based on susceptibility artifacts (dark spots on MRI) generated by intrinsic magnetic properties of the device. *Active* refers to incorporation of an MRI receiver coil (antenna, electrically connected to the scanner) into the catheter, which is sensitive to signal only from adjacent tissue and is used to create bright spots on the MR images.

The passive device was an unmodified 10 × 100 mm iliac limb of a commercial nitinol endograft (Vanguard, Boston Scientific, Natick, Massachusetts). A quarter-wave 0.030-inch active guidewire was used to enhance visualization of the passive endograft. All active devices were built by one of the investigators (P.V.K.). Endografts were constructed from 0.009-inch gold-plated nitinol wire in a Z-stent design, lined with thin expanded polytetrafluoroethylene and having diameters of 10 to 14 mm and lengths of 60 to 80 mm. Endografts were mounted on 5-F 65-cm nonferrous Kumpe catheters (Angiodynamics, Queensbury, New York), acting as delivery shafts, and crimped inside 10-F nylon sheaths (Fast-Cath, Daig, Minnetonka, Minnesota).

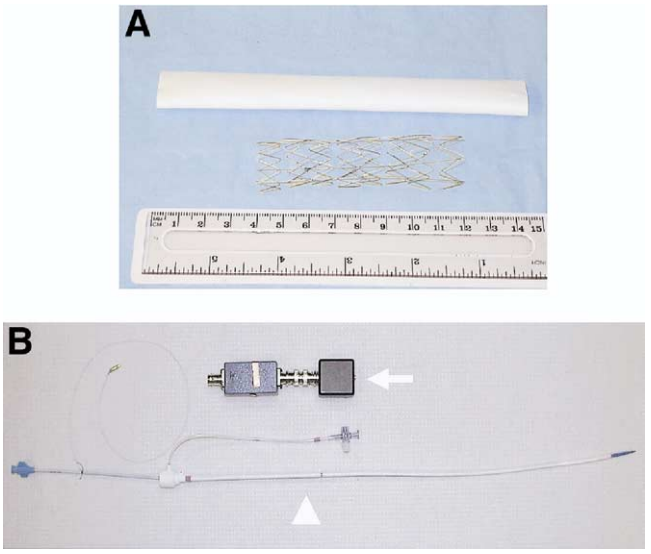


**Figure 1.** Active-stent endograft. **(A)** Components of homemade active endograft, constructed from 0.009-inch nitinol wire and expanded polytetrafluoroethylene graft material. **(B)** Completed one-channel active-stent device mounted on a 5-F catheter and constrained within a 10-F nylon sheath **(arrowhead)**. Matching tuning circuitry is housed in a separate box **(arrow)**.

Polyimide tubing improved the stiffness of the Kumpe delivery shaft and the ease of sheath retraction for endograft deployment (Fig. 1).

Schematics for the active devices are shown in Figure 2. The passive endograft is depicted in Figure 2A. An active-marker/passive-stent design (Fig. 2B) incorporated two opposed solenoid coils built into the delivery shaft at each edge of the stent, analogous to radiopaque end markers on X-ray systems. Another active-stent design incorporated a loopless antenna. The delivery shaft acted as ground, and the Z-stent served as antenna whip (region of antenna receiving signal), connected to the shaft by a wire (19–21) (Fig. 2C) and designed to detach after deployment. The final active-stent/active-marker system combined the loopless coil endograft with a separate loop coil wound around the delivery device's distal cone just beyond the stent itself (Fig. 2D). Decoupling circuitry was housed in external shielded boxes.

**ENDOGRAFT PHANTOM, HEATING, AND IN VIVO TESTING.** All active devices were imaged in saline phantoms before in vivo experiments to confirm signal and appearance.

Heating of the endograft was tested in vitro in a polyacrylamide gel phantom and in vivo in one additional animal. Conditions were intended to exaggerate heating, including continuous steady-state free precession (SSFP) scanning with a high flip angle (alpha = 75°, repetition time [TR] = 3.1 ms). Temperature was measured using four fiberoptic thermistor probes (Umi-4, Fiso Technologies, Quebec, Canada) placed along the length of the device, including the tip.

**FUNCTIONAL AND ANATOMIC MRI TECHNIQUES.** Functional MRI techniques included dynamic magnetic reso-

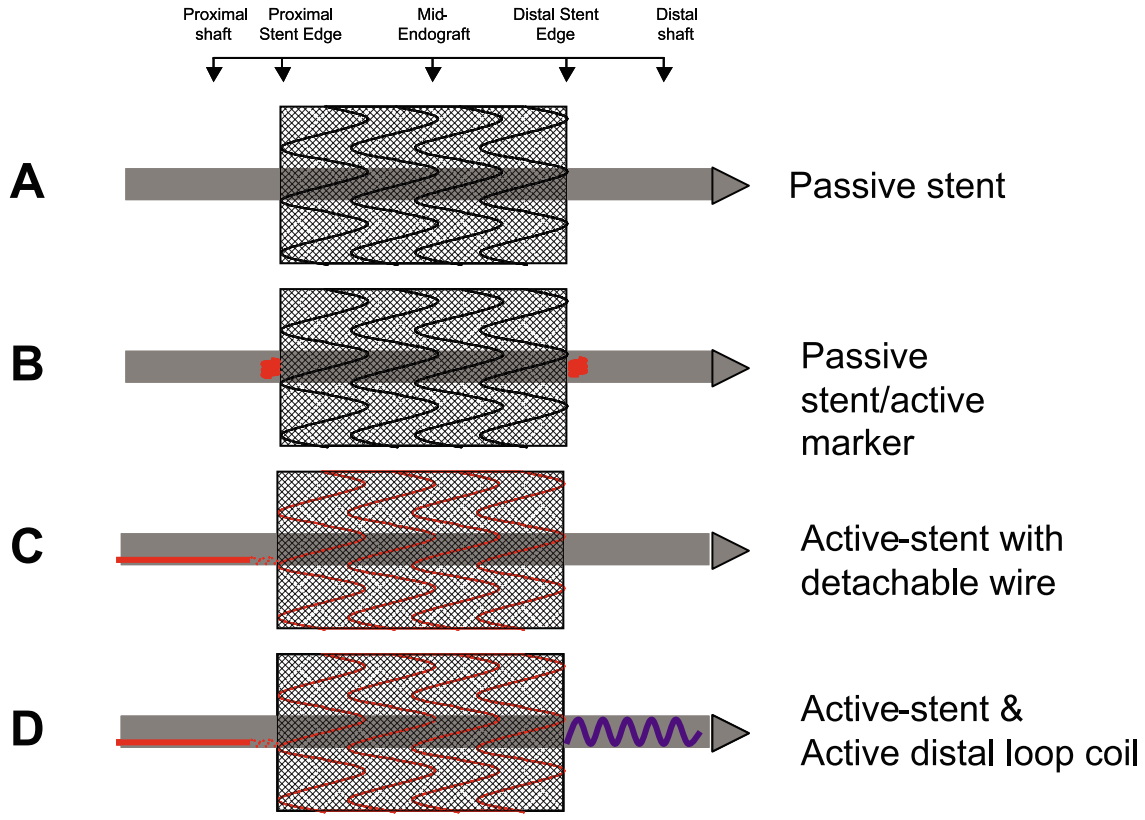


**Figure 2.** Schematic of endograft designs. **(A)** Unmodified commercial device imaged on the basis of intrinsic magnetic susceptibility (signal void). **(B)** Homemade endograft device with active opposed loop solenoid coils as markers delineating proximal and distal stent edges. **(C)** Homemade endograft device with active stent connected to delivery system shaft by a detachable cable that, after deployment and removal of the delivery catheter, renders the stent inactive. **(D)** Homemade endograft device with active stent as described in (C) and second active marker composed of a multilooped coil on the delivery shaft just beyond the distal stent edge.

nance angiography (MRA) and phase-contrast imaging. Immediately after aneurysm creation, animals were transferred to a co-located 1.5-T MRI scanner (Signa CV/I, General Electric, Waukesha, Wisconsin, or Sonata, Siemens, Erlangen, Germany) for imaging using 4- or 8-channel phased-array surface coils (NovaMedical, Wakefield, Massachusetts, or Siemens). Contrast-enhanced digital-subtraction MRA was performed with systemic injection of 0.1 to 0.2 mmol/kg gadopentate dimeglumine (Magnevist, Berlex, Wayne, New Jersey) with a 3D radiofrequency-spoiled gradient echo (SPGR) acquisition using the following parameters: repetition time (TR)/echo time (TE) 6.7/1.2 ms, flip angle 45°, matrix 512 × 192 × 24, field-of-view 36 × 27 × 8.2 cm, receiver bandwidth ±62.5 kHz, voxel size 0.7 × 1.4 × 3.4 mm. Mask, arterial, venous (after 60 s), and late phases (after 5 min) were obtained to identify slow contrast accumulation in the aneurysm sac. A 3D, low-flip-angle fast-gradient-echo scan with and without fat saturation was run with thin axial partitions delineating aortic anatomy before and after endograft deployment to assess stent strut apposition (TR/TE 5.8/1.2 ms, flip angle 15°, matrix 256 × 160 × 24, bandwidth 490 Hz/pixel, resolution 1.1 × 1.7 × 4 mm). Stent strut apposition was also confirmed on axial cuts using high-resolution rectilinear trajectory SSFP (matrix 256 × 256, field-of-view 20 × 20 cm, in-plane resolution 0.8 × 0.8 mm, slice thickness 6 mm) and reduced field-of-view (rFOV) radial trajectory SSFP (22) (TR/TE 4.5/2.3 ms, flip angle 60°, 32 projections with 17 interleaves, regridded to matrix 128 × 128, field-of-view 12 × 12 cm, slice thickness 6 mm, bandwidth 560 Hz/pixel), as well as black-blood fast spin echo (TR/TE 1200/100 ms, flip angle 180°, echo train length 16, matrix 384 × 256, field-of-view 30 × 20 cm, slice thickness 5 mm, bandwidth ±62.5 kHz, in-plane resolution 0.8 × 0.8 mm).

Phase-contrast imaging was used qualitatively to assess flow perturbations within the aneurysm before and after endograft deployment. Flow velocities were assessed along three axes using in-plane and through-plane phase-contrast scans (TR/TE 5.0/3.0 ms, matrix 192 × 96, field-of-view 32 × 24 cm, slice thickness 5 mm, bandwidth ± 62.5 kHz, resolution 2.5 × 2.5 mm, through-plane velocity encoding 150 cm/s, in-plane velocity encoding 80 cm/s). Phase-contrast data were represented with through-plane flow mapped as color, and in-plane flow was mapped as velocity vectors (MATLAB, Mathworks, Natick, Massachusetts) (23).

**Real-time MRI and interventional procedure.** The rtMRI for procedural guidance required several modifications to commercial hardware and software, including external image reconstruction and in-room display, as previ-

ously described (17,24,25). Interactive rtMRI user interfaces were customized with the addition of several useful features for rectilinear SSFP imaging (25,26): individual receiver channel gain, coloring, and highlighting for use with active intravascular devices; preparatory saturation pulses to negate signal from fat or specific spatial regions; simultaneous acquisition and display of multiple image slices; and real-time 3D rendering of multislice data (25). An interactive point marking system was implemented allowing user-selected reference points on individual slices to be represented on the 3D rendering. This was useful, for example, to mark visceral artery ostia. A parallel real-time environment used radial k-space trajectories, a data-undersampling technique that optimizes temporal resolution without sacrificing spatial resolution (22). This interface was also customized to allow interactive overlay of previously acquired angiographic roadmaps.

Typical real-time SSFP imaging used the following parameters: TR/TE 3.8/1.8 ms, matrix 192 × 128, flip angle 60°, slice thickness 8 mm, field-of-view 36 × 24 cm, bandwidth ±64 to 128 kHz. Image position could be adjusted interactively by drawing new prescriptions on the current image, pushing or pulling through parallel planes by user-specified gap thickness, and rotating vertically or horizontally around the image center by user-specified angle increments. These yielded four to eight frames/s, depending on whether image acceleration techniques such as echo sharing were used. The imaging latency, or time to acquire, reconstruct, and display images to the operator using this system is approximately 250 ms.

**Corroboration of aneurysm exclusion.** After endograft deployment and post-procedural MR anatomic and functional imaging as described for baseline studies, X-ray subtraction angiography was repeated. Animals were euthanized, and the abdominal aorta was excised for visual inspection in six.

## RESULTS

**Aneurysm model.** Balloon overstretch dilation of the infrarenal aorta was performed successfully in all 11 animals. Perforation/rupture of the aorta occurred in two, but both survived for the duration of the nonsurvival experimental protocol. At the widest, dilated segments were up to twice the reference aortic diameters. In all cases, aneurysms persisted throughout the experimental protocol, up to 6 h, usually without significant recoil.

**Endograft testing.** In vitro all active devices showed enhanced signal in the immediately surrounding region. However, the receiver coil on the active-marker/passive-stent device (Fig. 2B) coupled inductively with the nitinol stent, resulting in increased signal along the entire device rather than discretely at each end-marker coil. There was marked signal drop-off within 2 to 3 mm of the distal end of the active-stent devices (Fig. 2C), a known limitation of the loopless antenna design (20). The active-stent/active-marker design (Fig. 2D) overcame this limitation by placing a loop coil (27) to act as an edge marker distal to the stent.

Heating was only noted at the tip. The maximum temperature increase was 2.0°C in the in vitro static phantom, and 2.2°C in vivo.

Signal-to-noise profiles of the final endograft design, combining an active stent with active edge markers, was higher than for all previous designs, and contrast-to-noise for the final device was different primarily at the endograft edges (data not shown).

**Real-time MR guidance of endograft procedures.** Real-time imaging with SSFP provided adequate temporal resolution for device navigation, positioning, and deployment. Spatial resolution was sufficient to visualize important visceral and branch artery origins necessary for precise device placement.

In one of the animals with aortic rupture, the rapidly accumulating retroperitoneal hematoma obscured important anatomy. This problem was circumvented by thick-slice, real-time angiography with a hand injection of dilute (30 mM) gadolinium contrast during image acquisition. Active devices were easily visualized within the aorta using color highlighting and individual channel gain adjustment.

Multislice imaging provided reference coronal and sagittal slices of the infrarenal aorta with renal and iliac vessels while allowing interactive adjustment of axial slices to verify and adjust device position. The slices were displayed individually and in combination after real-time 3D rendering (Figs. 3A and 3B). A point marking system allowed precise delineation of important anatomic references, including proximal and distal aneurysm extent, with display on the 3D image to guide device positioning and deployment (Fig. 3A).

The balance between spatial resolution, the number of image slices, and temporal resolution was adjusted iteratively, in combination with temporal filtering and multiplanar imaging. Optimal anatomic guidance seemed to be provided by multiple (3–5) non-orthogonal slices, each fully refreshed only approximately once per second.

**Performance of different MRI-endograft designs.** The commercial endograft system (Fig. 2A, one tested) was visualized passively by its marked susceptibility artifact, but this made it very difficult to differentiate the stent itself from the delivery shaft. We attempted to improve device visualization by inserting a quarter-wave active antenna-guidewire through the lumen of the endograft system. This enhanced local signal but did not satisfactorily delineate the device.

The active-marker/passive-stent device (Fig. 2B, one tested) showed bright signal along the length of the device rather than discretely at the markers only. The distal edge of the stent could not definitively be identified. Additionally, the tip of the delivery system, extending 2 cm beyond the distal active marker, was not conspicuous because of volume averaging.

The loopless coil design of the active-stent device (Fig. 2C, two tested) provided good signal except along the distal

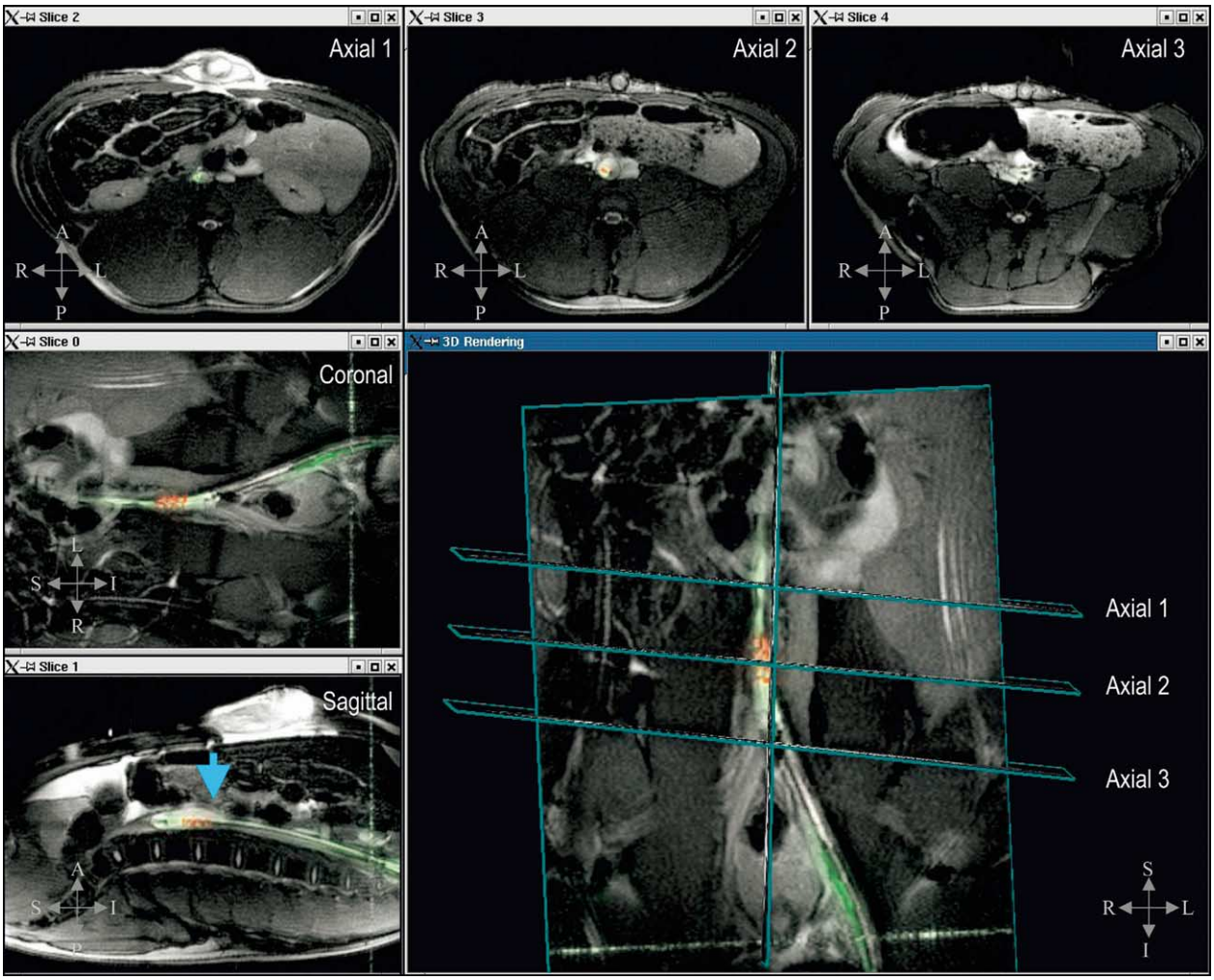


**Figure 3.** Real-time multislice imaging and three-dimensional rendering during endograft positioning. In the **left column**, real-time magnetic resonance imaging multislice axial, sagittal, and coronal images shown simultaneously facilitate precise device positioning. Concomitant three-dimensional rendering on the **right** integrates multislice information. Positioning three axial slices at the caudal renal artery origin, the middle of the aneurysm, and the aortic bifurcation, respectively, allows simultaneous capture of the most important anatomy for device placement. The coronal and sagittal slices provide an overall "bird's eye" view of the aorta. Orientation markers indicate: S = superior, I = inferior, A = anterior, P = posterior, R = right, L = left. **Blue arrow** indicates aneurysm.

several millimeters of the actual endograft, reducing operator confidence during positioning and deployment.

The final device iteration combined an active stent with an active distal loop coil at the distal tip of the delivery catheter (Fig. 2D, seven tested). This design produced the most reproducible signal pattern and provided satisfactory operator confidence in device position.

The two procedural failures were attributed to the fragility of these homemade prototypes, built primarily for imaging rather than mechanical characteristics. Of the two procedural failures, one was related to shifting of the self-expanding endograft during unsheathing, and the other was related to migration during withdrawal of the detachable antenna connection.

**MR assessment of procedural success.** Nine of 11 endograft procedures were successful under rtMRI guidance. The two failures were identified using first-pass MRA. No attempt was made to correct acute endoleaks using adjunctive balloon or stent devices.

Stent strut apposition at the proximal and distal target segments of the aorta was convincingly shown by high-resolution axial SSFP, fast spin echo, and 3D gradient echo scans (Fig. 4).

Repeat MRA in 9 of 11 cases showed both aneurysm exclusion by the endograft (Fig. 5) and patency of the renal arteries. Iliac arteries were also patent by angiography. Successful exclusion was further corroborated by lack of contrast accumulation in the aneurysm sac during late-phase angiographic and real-time SSFP scans. In the other two cases, MR contrast-angiography revealed procedural failure with evidence of gadolinium within the aneurysm sac.

High-resolution phase-contrast studies with vector- and color-flow mapping showed reduction of in-plane and through-plane turbulence consistent with restoration of laminar flow (Fig. 6). In the two procedural failures, phase contrast imaging was not specifically conducted to iden-

JACC Vol. 45, No. 12, 2005
June 21, 2005:2069–77

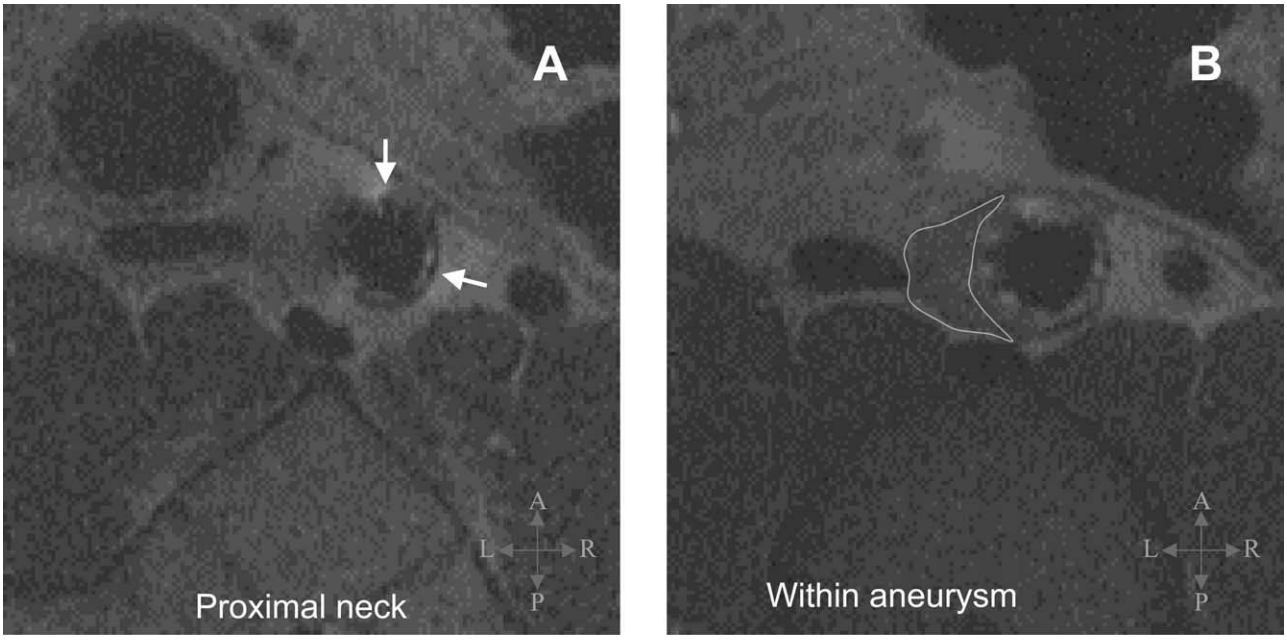


**Figure 4.** Stent strut apposition. **(A)** Fast spin echo image shows nitinol stent well apposed to target proximal infrarenal aorta (**arrows** show signal void from stent struts). **(B)** Spin-echo axial image at level of aneurysm, showing excluded sac **(dashed outline)**. Orientation markers as in Figure 3.

tify flow jets associated with endoleaks identified by contrast MRA.

**X-ray angiography and pathology.** Digital subtraction angiography corroborated MRA findings in all nine cases deemed successful by MRI. Direct inspection and palpation of the resected abdominal aorta in six successful cases confirmed that the renal arteries were not involved.

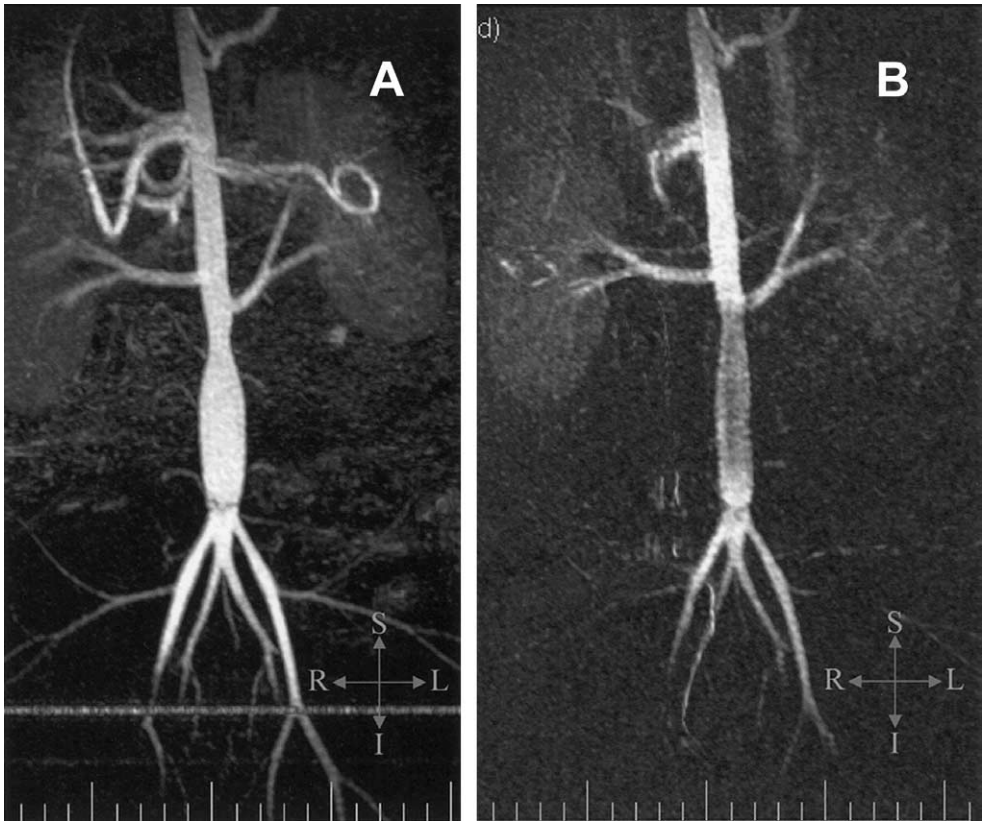


**Figure 5.** Magnetic resonance angiogram (maximum-intensity projection) before and after endograft delivery. **(A)** Conventional contrast-enhanced magnetic resonance angiography shows infrarenal abdominal aortic aneurysm after balloon overstretch. **(B)** Abdominal aortic aneurysm is excluded by nitinol endograft (causing luminal artifact). Orientation markers as in Figure 3.

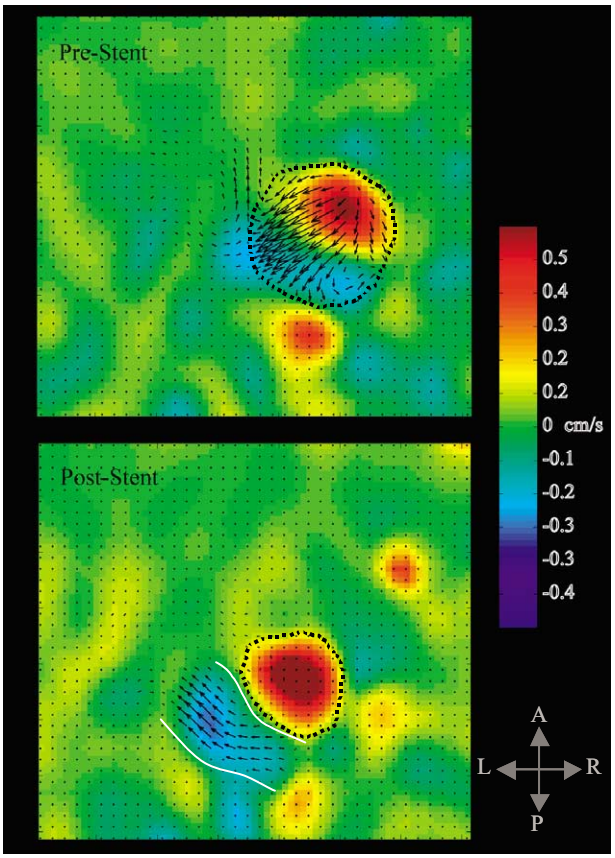


**Figure 6.** Phase-contrast flow assessments before and after endograft deployment. Axial overlays of in-plane (vector flow map) and through-plane (color map) flow within ruptured experimental aneurysm. Before endovascular repair, there is marked turbulence and evidence of retrograde flow **(blue)** within the aneurysm **(dashed outline)**. The vena cava is collapsed in this hemorrhagic state. Laminar flow is restored after endograft **(dashed outline)** deployment. **Solid lines** border vena cava, identified on cine loops by constant nonpulsatile flow. Orientation markers as in Figure 3.

## DISCUSSION

We showed the feasibility of endovascular repair of AAA performed entirely under real-time MRI guidance in a swine model. Functional imaging with dynamic contrast MRA and phase-contrast techniques complemented the anatomic imaging for immediate assessment of procedural success.

**Endograft devices and MRI.** Our approach to devices encompassed both passive and active designs for visualization and tracking. The unmodified, commercial passive endograft was difficult to differentiate from the delivery system, limiting operator confidence in positioning and deployment. Moreover, signal voids generated by passive devices cannot be readily distinguished from signal attenuation of other causes or from volume averaging (28). Because active devices function as receiver coils, the resulting local signal enhancement markedly facilitates visualization (Figs. 3 and 4) (21,26,27,29). Mahnken et al. (30) positioned passive commercial endografts below renal arteries in healthy swine under MRI guidance, but also concluded that dedicated MRI endograft designs might be superior. We constructed several different types of homemade active endograft systems, of which the final two-channel conductively coupled active-marker/active-stent device provided the most useful signal profile.

The rtMRI with SSFP provided excellent intrinsic blood contrast within the aorta and its branch vessels, allowing optimal slice selection for the procedure. Unlike coronary and intracardiac procedures, in which ultrafast imaging is a prerequisite because of cardiac and respiratory motion, peripheral endovascular repair under MR guidance may be undertaken with slower frame rates that allow better spatial resolution. Radial k-space acquisition seems well suited to transcatheter aneurysm therapy because of advantages in rFOV imaging and because of intrinsic edge enhancement (22). Customized features on the interactive real-time interface proved very useful during the interventional procedure, particularly in channel coloring and gain adjustment to highlight and contrast the device from surrounding tissue. Multislice imaging with simultaneous real-time 3D rendering facilitated device positioning and deployment with complementary orthogonal and/or oblique views. Our ability to precisely position and deploy the endografts was good and was limited only by the mechanical shortcomings of our homemade devices.

Post-deployment scanning combined anatomic and functional assessment of procedural success. High-resolution, rFOV SSFP, fast spin echo and 3D gradient echo scans convincingly showed stent strut apposition to the proximal and distal target aortic segments. Dynamic contrast-enhanced MRA during arterial, venous, and late phases corroborated aneurysm exclusion in successful cases and clearly showed contrast accumulation in the aneurysm sac after procedural failures. Phase-contrast scans visually showed restoration of laminar flow in the grafted segment.

These studies were readily completed within minutes of endograft delivery.

**Study limitations and clinical implications for endovascular repair.** Although we successfully excluded aneurysmal segments immediately in all cases in which the homemade device functioned appropriately, our experience should be qualified. We used a model of AAA in healthy, nonatherosclerotic swine. Even after balloon overstretch injury, the course of the infrarenal aorta remained essentially unchanged. This and more complicated surgical models cannot represent the complex 3D anatomy and tortuosity encountered clinically in degenerative arterial segments in patients with AAA, in whom the expected benefits of detailed soft tissue contrast and 3D representation by MRI may be more dramatic. In particular, safe traversal of tortuous iliac artery segments, one of the procedural challenges of AAA endografting, might be simplified by using rtMRI to visualize device-related anatomic distortion and to guide operator adjustments. Furthermore, we used a simple tubular endograft, although most clinical devices are bifurcated to cover the aorta and both iliac limbs.

Our experience suggests that an active endograft design would be most appropriate for further clinical development. Despite iterative prototype testing, the optimal device design remains undetermined. Additional issues include whether an endograft system with associated invasive equipment (e.g., guidewires) made from nonferrous materials retains adequate mechanical characteristics to traverse tortuous and/or calcified iliac arteries. Inductive heating during radiofrequency excitation is an important safety consideration for long conductive catheter devices in MRI. Our prototype devices showed minimal local heating because of decoupling circuitry to limit radiofrequency energy deposition. This is amenable to further optimization (31,32).

Although AAA endografting has emerged over the past decade as a viable alternative to open surgery, failure modes such as malapposition could conceivably be improved using MRI for on-line planning, procedural guidance, and immediate post-procedural assessment. The rtMRI might improve procedural success by improving soft-tissue and 3D imaging during the procedure. The SSFP provides intrinsic contrast for excellent visualization of the aorta and major branch vessels without exogenous agents. Substituting gadolinium-based MR contrast for iodinated radiocontrast agents might reduce contrast nephropathy in this at-risk clinical population (33). Magnetic resonance imaging may facilitate device selection by improving the measurement accuracy of aneurysm neck dimension, in which oversizing has been associated with endograft displacement and migration (10). Furthermore, aneurysm anatomy may be altered by the use of a stiff guidewire and introduction of a bulky, high-profile endograft delivery system. Interactive MRI may offer better delineation of this complex intraprocedural anatomy than conventional X-ray projection imaging. Finally, combined on-line anatomic and functional MRI may be useful for guiding and evaluating procedural success. The chief obstacle to clinical translation of our findings is the unavailability of clinical-grade commercial active MRI endografts.

## CONCLUSIONS

These experiments show that successful endovascular repair of experimental AAA in swine can be conducted solely under rtMRI. Endografts can be built to be conspicuous during the procedure. Anatomic and complementary functional MRI can guide graft deployment and can immediately assess procedural success. Although significant future development of active devices is required, we believe this represents an attractive application for cardiovascular MR-guided intervention.

**Reprint requests and correspondence:** Dr. Robert J. Lederman, Cardiovascular Branch, Clinical Research Program, Division of Intramural Research, National Heart, Lung, and Blood Institute, National Institutes of Health, Building 10, Room 2c713, Bethesda, Maryland 20892-1538. E-mail: Lederman@nih.gov.

## REFERENCES

1. Buth J. Endovascular repair of abdominal aortic aneurysms. Results from the EUROSTAR registry. EUROpean collaborators on stent-graft techniques for abdominal aortic aneurysm repair. Semin Interv Cardiol 2000;5:29–33.
2. Matsumura JS, Brewster DC, Makaroun MS, Naftel DC. A multicenter controlled clinical trial of open versus endovascular treatment of abdominal aortic aneurysm. J Vasc Surg 2003;37:262–71.
3. Zarins CK, White RA, Moll FL, et al. The AneuRx stent graft: four-year results and worldwide experience 2000. J Vasc Surg 2001; S33:135–45.
4. White GH, Yu W, May J, Chaufour X, Stephen MS. Endoleak as a complication of endoluminal grafting of abdominal aortic aneurysms: classification, incidence, diagnosis, and management. J Endovasc Surg 1997;4:152–68.
5. May J, White GH, Waugh R, et al. Adverse events after endoluminal repair of abdominal aortic aneurysms: a comparison during two successive periods of time. J Vasc Surg 1999;29:32–7; discussion 38–9.
6. Veith FJ, Baum RA, Ohki T, et al. Nature and significance of endoleaks and endotension: summary of opinions expressed at an international conference. J Vasc Surg 2002;35:1029–35.
7. Alric P, Hinchliffe RJ, Wenham PW, Whitaker SC, Chuter TA, Hopkinson BR. Lessons learned from the long-term follow-up of a first-generation aortic stent graft. J Vasc Surg 2003;37:367–73.
8. Tzortzis E, Hinchliffe RJ, Hopkinson BR. Adjunctive procedures for the treatment of proximal type I endoleak: the role of peri-aortic ligatures and Palmaz stenting. J Endovasc Ther 2003;10:233–9.
9. Tummala S, Powell A. Imaging of endoleaks. Tech Vasc Interv Radiol 2001;4:208–12.
10. Badran MF, Gould DA, Raza I, et al. Aneurysm neck diameter after endovascular repair of abdominal aortic aneurysms. J Vasc Interv Radiol 2002;13:887–92.
11. Thurnher SA, Dorffner R, Thurnher MM, et al. Evaluation of abdominal aortic aneurysm for stent-graft placement: comparison of gadolinium-enhanced MR angiography versus helical CT angiography and digital subtraction angiography. Radiology 1997;205:341–52.
12. Ludman CN, Yusuf SW, Whitaker SC, Gregson RH, Walker S, Hopkinson BR. Feasibility of using dynamic contrast-enhanced magnetic resonance angiography as the sole imaging modality prior to endovascular repair of abdominal aortic aneurysms. Eur J Vasc Endovasc Surg 2000;19:524–30.
13. Cejna M, Loewe C, Schoder M, et al. MR angiography vs CT angiography in the follow-up of nitinol stent grafts in endoluminally treated aortic aneurysms. Eur Radiol 2002;12:2443–50.
14. Razavi R, Hill DL, Keevil SF, et al. Cardiac catheterisation guided by MRI in children and adults with congenital heart disease. Lancet 2003;362:1877–82.
15. Buecker A, Spuentrup E, Grabitz R, et al. Magnetic resonance-guided placement of atrial septal closure device in animal model of patent foramen ovale. Circulation 2002;106:511–5.
16. Rickers C, Jerosch-Herold M, Hu X, et al. Magnetic resonance image-guided transcatheter closure of atrial septal defects. Circulation 2003;107:132–8.
17. Dick AJ, Guttman MA, Raman VK, et al. Magnetic resonance fluoroscopy allows targeted delivery of mesenchymal stem cells to infarct borders in swine. Circulation 2003;108:2899–904.
18. Hallisey MJ. 1997 SCVIR Gary J. Becker Young Investigator Award paper. A transluminally created abdominal aortic aneurysm model. J Vasc Interv Radiol 1997;8:305–12.
19. Quick HH, Ladd ME, Nanz D, Mikolajczyk KP, Debatin JF. Vascular stents as RF antennas for intravascular MR guidance and imaging. Magn Reson Med 1999;42:738–45.
20. Ocali O, Atalar E. Intravascular magnetic resonance imaging using a loopless catheter antenna. Magn Reson Med 1997;37:112–8.
21. Ladd ME, Zimmermann GG, Quick HH, et al. Active MR visualization of a vascular guidewire in vivo. J Magn Reson Imaging 1998;8:220–5.
22. Peters DC, Lederman RJ, Dick AJ, et al. Undersampled projection reconstruction for active catheter imaging with adaptable temporal resolution and catheter-only views. Magn Reson Med 2003;49:216–22.
23. Thompson RB, McVeigh ER. High temporal resolution phase contrast MRI with multiecho acquisitions. Magn Reson Med 2002;47: 499–512.

24. Guttman MA, McVeigh ER. Techniques for fast stereoscopic MRI. Magn Reson Med 2001;46:317–23.
25. Guttman MA, Lederman RJ, Sorger JM, McVeigh ER. Real-time volume rendered MRI for interventional guidance. J Cardiovasc Magn Reson 2002;4:431–42.
26. Lederman RJ, Guttman MA, Peters DC, et al. Catheter-based endomyocardial injection with real-time magnetic resonance imaging. Circulation 2002;105:1282–4.
27. Serfaty JM, Yang X, Aksit P, Quick HH, Solaiyappan M, Atalar E. Toward MRI-guided coronary catheterization: visualization of guiding catheters, guidewires, and anatomy in real time. J Magn Reson Imaging 2000;12:590–4.
28. Bakker CJ, Bos C, Weinmann HJ. Passive tracking of catheters and guidewires by contrast-enhanced MR fluoroscopy. Magn Reson Med 2001;45:17–23.
29. Atalar E, Bottomley PA, Ocali O, et al. High resolution intravascular MRI and MRS by using a catheter receiver coil. Magn Reson Med 1996;36:596–605.
30. Mahnken AH, Chalabi K, Jalali F, Gunther RW, Buecker A. Magnetic resonance-guided placement of aortic stents grafts: feasibility with real-time magnetic resonance fluoroscopy. J Vasc Interv Radiol 2004;15:189–95.
31. Yeung CJ, Susil RC, Atalar E. RF heating due to conductive wires during MRI depends on the phase distribution of the transmit field. Magn Reson Med 2002;48:1096–8.
32. Susil RC, Yeung CJ, Atalar E. Intravascular extended sensitivity (IVES) MRI antennas. Magn Reson Med 2003;50:383–90.
33. Spinosa DJ, Kaufmann JA, Hartwell GD. Gadolinium chelates in angiography and interventional radiology: a useful alternative to iodinated contrast media for angiography. Radiology 2002;223:319–25; discussion 326–7.